




## Scalar potentials for light in a cavity

K. J. H. Peters <sup>1</sup>, J. Busink,<sup>1</sup> P. Ackermans,<sup>1</sup> K. G. Cognée,<sup>2</sup> and S. R. K. Rodriguez <sup>1,\*</sup>

<sup>1</sup>Center for Nanophotonics, AMOLF, Science Park 104, 1098 XG Amsterdam, The Netherlands

<sup>2</sup>Center for Discovery and Innovation, City College of New York, New York, New York 10031, USA

 (Received 13 September 2022; revised 19 January 2023; accepted 25 January 2023; published 27 February 2023)

The nonequilibrium dynamics of light in a coherently driven nonlinear cavity resembles the equilibrium dynamics of a Brownian particle in a scalar potential. This resemblance has been known for decades, but the correspondence between the two systems has never been properly assessed. Here we demonstrate that this correspondence can be exact, be approximate, or break down, depending on the driving conditions. For vanishing nonlinearity and on-resonance driving, the correspondence is exact: The cavity dissipation and driving amplitude define a scalar potential, and light follows the equilibrium Boltzmann distribution with an effective temperature defined by the noise variance and cavity dissipation. The scalar potential pertaining to linear on-resonance dynamics fails dramatically in nonlinear and/or off-resonance regimes. However, we introduce a distinct scalar potential enabling an effective equilibrium description of light. Our potential gives a reasonably accurate description in limited nonlinear regimes of bistability, but fails deep in the bistability where nonconservative forces dominate the dynamics. Consequently, the correspondence to Brownian motion in a scalar potential breaks down. This breakdown is accompanied by a qualitative change in the spectrum of small intracavity field fluctuations, reminiscent of an exceptional point of a non-Hermitian Hamiltonian. Our results lay the foundations for an effective thermodynamic description of coherently driven cavities, and suggest that fundamental results for overdamped Langevin dynamics can help to assess the energetics and information processing of resonant optical technologies.

DOI: [10.1103/PhysRevResearch.5.013154](https://doi.org/10.1103/PhysRevResearch.5.013154)

### I. INTRODUCTION

Many advances in physics have resulted from identifying a correspondence between nonequilibrium behavior of light and equilibrium behavior of matter. For example, Haken realized that lasing corresponds to a second-order phase transition in equilibrium [1]. He furthermore connected optics to Ginzburg-Landau theory [1,2], and thereby pioneered research on phase transitions of photons. This research has flourished recently, resulting, for example, in the discovery of dissipative phase transitions [3–9] and applications to quantum technologies [10–13]. A more recent example is due to Foss-Feig and co-workers, who described a bistable cavity array as a classical Ising model in equilibrium [14]. This correspondence is promising for solving nondeterministic polynomial time ( $NP$ )-hard problems [15,16], for which no efficient algorithm exists [17].

In the 1980s, Risken and co-workers made an interesting analogy between light in a bistable cavity and Brownian motion in a double-well potential [18–20]. They associated optical states with potential minima, and light fluctuations

with thermal motion. Despite the long history of this analogy, its exact or approximate validity has never been properly assessed. Recently, Andersen and co-workers defined a scalar potential for a bistable resonator [21]. Using their scalar potential and the equilibrium theory of Kramers [22], they approximately reproduced the system's dynamics in certain parameter regimes. In other regimes, inconsistencies with quantum theory were attributed to quantum effects rather than to the questionable validity of their scalar potential. This prompts the questions: Can a scalar potential capture optical dynamics in a cavity? And how far does the correspondence to equilibrium physics go? Figure 1 illustrates the essence of these questions, which motivate this work.

Here we demonstrate that the correspondence between stochastic light in a coherently driven single-mode cavity and equilibrium Brownian dynamics in a one-dimensional (1D) scalar potential can be exact, be approximate, or break down, depending on the optical system's parameters. The exact, approximate, and breakdown regimes are not trivial extensions of each other. Actually, the intermediate regime admitting an approximate equilibrium description is based on a scalar potential we introduce, and which is very different from the potential in the exact correspondence regime. This paper is organized as follows. In Sec. II we introduce the model for a single-mode nonlinear cavity. We then show that a single electromagnetic mode is mathematically equivalent to two-dimensional overdamped Langevin dynamics under a nonconservative force which cannot be derived from a scalar potential. It turns out that this nonconservative force can

\*s.rodriguez@amolf.nl

Published by the American Physical Society under the terms of the [Creative Commons Attribution 4.0 International license](https://creativecommons.org/licenses/by/4.0/). Further distribution of this work must maintain attribution to the author(s) and the published article's title, journal citation, and DOI.

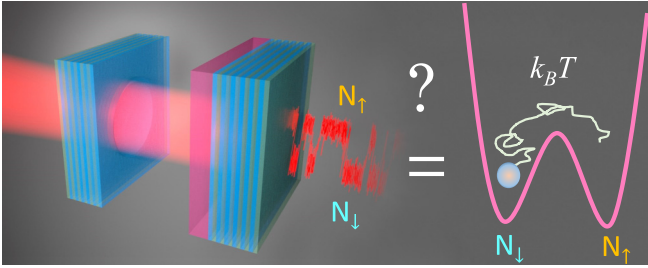


FIG. 1. Left: The transmission of a coherently driven nonlinear optical cavity switches between two states due to the influence of noise. Right: A Brownian particle in a scalar double-well potential. The figure, overall, illustrates the main question motivating this paper: Is stochastic light in a coherently driven cavity a Brownian particle in a scalar potential?

vanish in two ways, one discussed in Sec. III and another discussed in Sec. IV. However, only the way discussed in Sec. III allows an exact effective equilibrium description in terms of a scalar potential. In an attempt to *approximately* describe nonlinear optical dynamics in terms of a scalar potential, in Sec. V we identify a path in the two-dimensional (2D) phase space along which we define a 1D scalar potential. In Sec. VI we assess the accuracy of this 1D potential by comparing its corresponding equilibrium distribution with the distribution of the 2D system along the same path. We make this comparison across the monostable-to-bistable transition, and find nonmonotonic deviations from effective equilibrium behavior across the transition. We also show that the strength of the noise has a nontrivial effect on these deviations. In Sec. VII we explain the validity range of our approximate 1D potential by analyzing the spectrum of small fluctuations on top of the steady-state cavity field. We find a qualitative change in the fluctuation spectrum at the boundary of the validity range of our potential. This change occurs at a point reminiscent of the exceptional point of a non-Hermitian Hamiltonian. The models we relate—the overdamped Langevin equation and a single-mode coherently driven cavity—are cornerstones of stochastic thermodynamics on one hand and resonant optics on the other hand. While connections between classical (deterministic) thermodynamics and optics have been known for decades [23], our results point to a frontier at the intersection of *stochastic* thermodynamics [24–27] and resonant optics. Section VIII presents our perspective towards that frontier and a summary of our results.

## II. THE MODEL

We consider a coherently driven single-mode cavity with cubic nonlinearity. This paradigmatic system is at the heart of recent studies of dissipative phase transitions [4–6,8,28–31], polariton blockade [32,33], and stochastic resonance [34,35]. Single-mode cavities are also intensely investigated for applications to sensing [36–40], nanoparticle trapping [41], nonreciprocity [42–48], and quantum technologies [49–51].

The state of the cavity can be described exactly based on a master equation or the corresponding Fokker-Planck equation, as shown by Drummond and Walls [52]. Here we make an equivalent (under the assumptions given in Appendix A)

description based on a stochastic differential equation in the spirit of Langevin’s celebrated equation [53]. Such a description is well suited for elucidating Brownian motion [54], and for exploring the properties of stochastic trajectories which are solutions to the Langevin equation for a particular noise realization [55,56].

In a frame rotating at the frequency  $\omega$  of the driving laser, the intracavity light field  $\alpha$  satisfies

$$i\dot{\alpha} = \left(-\Delta - i\frac{\Gamma}{2} + U|\alpha|^2\right)\alpha + i\sqrt{\kappa_L}A + D\zeta(t). \quad (1)$$

$\Delta = \omega - \omega_0$  is the laser’s detuning from the resonance frequency  $\omega_0$ .  $\Gamma = \gamma_a + \kappa_L + \kappa_R$  is the total loss rate, with  $\gamma_a$  the absorption rate and  $\kappa_{L,R}$  a “left” or “right” input-output rate.  $U$  is the Kerr nonlinearity strength.  $A$  is the laser amplitude, assumed to be real.  $\zeta(t) = \zeta_R(t) + i\zeta_I(t)$  is a complex-valued stochastic term accounting for white noise in the laser amplitude and phase.  $\zeta_{R,I}$  are each a Gaussian process with mean  $\langle \zeta_R(t) \rangle = \langle \zeta_I(t) \rangle = 0$  and correlation  $\langle \zeta_j(t)\zeta_k(t') \rangle = \delta_{j,k}\delta(t')$ . Since each Gaussian process  $\zeta_{R,I}$  has standard deviation equal to one,  $D$  is the standard deviation of each stochastic force  $D\zeta_{R,I}$ . In Appendix A we discuss the assumptions and approximations underlying Eq. (1). Therein, we also refer to several experiments which are extremely well described by Eq. (1), with the noise properties we assume [5,34,35,57,58].

Let us decompose Eq. (1) into real and imaginary parts. Defining  $\alpha = \alpha_R + i\alpha_I$  and  $\Omega = UN - \Delta$  with  $N = |\alpha|^2$  the number of intracavity photons, we get

$$\begin{pmatrix} \dot{\alpha}_R \\ \dot{\alpha}_I \end{pmatrix} = \begin{pmatrix} -\frac{\Gamma}{2} & \Omega \\ -\Omega & -\frac{\Gamma}{2} \end{pmatrix} \begin{pmatrix} \alpha_R \\ \alpha_I \end{pmatrix} + \begin{pmatrix} \sqrt{\kappa_L}A \\ 0 \end{pmatrix} + D \begin{pmatrix} \zeta_R(t) \\ \zeta_I(t) \end{pmatrix}. \quad (2)$$

Equation (2) resembles a two-dimensional overdamped Langevin equation (OLE). In more than one dimension, the OLE has the form

$$\gamma \frac{d}{dt} \vec{x} = \vec{F} + D\vec{\xi}(t), \quad (3)$$

with  $\vec{F}$  a deterministic force matrix,  $\vec{\xi}(t)$  a stochastic force vector, and  $\gamma$  the damping which we assume to be equal for all degrees of freedom. Let us multiply Eq. (2) by  $\Gamma$  to make its left-hand side identical to that of Eq. (3). Then, we can identify the components of  $\vec{F}$  in our cavity:

$$F_R = \frac{-\Gamma^2\alpha_R}{2} + \Gamma\Omega\alpha_I + \Gamma\sqrt{\kappa_L}A, \quad (4a)$$

$$F_I = \frac{-\Gamma^2\alpha_I}{2} - \Gamma\Omega\alpha_R. \quad (4b)$$

For a scalar potential  $V = -\int \vec{F} d\vec{\alpha}$  to exist,  $\vec{F}$  must be conservative and irrotational. Its curl should vanish. Using the above expressions for  $F_R$  and  $F_I$ , we can calculate the magnitude of the curl of  $\vec{F}$  as follows:

$$|\vec{\nabla} \times \vec{F}| = \left| \left( \frac{\partial F_I}{\partial \alpha_R} - \frac{\partial F_R}{\partial \alpha_I} \right) \right| = \Gamma|2\Delta - 4UN|. \quad (5)$$

Hence,  $V$  can only exist if  $2\Delta = 4UN$  such that  $\vec{F}$  is irrotational. This condition can be satisfied in two ways. The first way, considered in Sec. III, is by driving a linear cavity on resonance such that  $\Delta = U = 0$ . The second way, considered

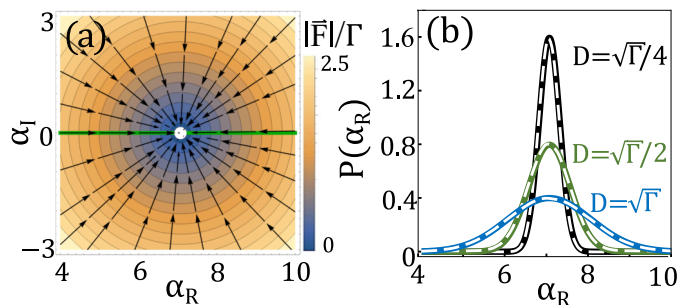


FIG. 2. (a) Phase portrait of a linear cavity driven on resonance.  $\alpha_R$  and  $\alpha_I$  are the real and imaginary parts of the intracavity field  $\alpha$ , respectively. Color and arrows represent force magnitude and direction, respectively. The white dot is the sole stable fixed point. (b) Probability density function of  $\alpha_R$  for three values of the standard deviation of the noise  $D$  relative to the dissipation  $\Gamma$ . Solid curves are numerical results using Eq. (1). Dashed white curves are Boltzmann distributions. The potential  $V_R$  for the Boltzmann distributions is defined along the green line in (a), where  $\alpha_I = 0$ . The effective temperature is given by  $T = \Gamma D^2 / 2k_B$ , with  $k_B$  the Boltzmann constant.

in Sec. IV, is by driving a nonlinear cavity off resonance with a laser amplitude giving  $N = \Delta / 2U$ .

### III. EXACT POTENTIAL FOR A LINEAR CAVITY DRIVEN ON RESONANCE

Consider a linear cavity driven on resonance, where  $\Omega = 0$  and  $\alpha_R$  decouples from  $\alpha_I$ . Figure 2(a) shows the phase portrait of this system. The magnitude and direction of  $\vec{F}$  are encoded in color and arrows, respectively. All force vectors are perpendicular to the contours of constant force magnitude and directed to the fixed point. This behavior is known as gradient flow. It arises when the system's dynamics are fully prescribed by a conservative force which is the negative gradient of a scalar potential.

Let us now integrate the forces in Eq. (4) (with  $\Omega = 0$ ) to obtain the corresponding scalar potentials:

$$V_R = \frac{\Gamma^2}{4} \alpha_R^2 - \Gamma \sqrt{\kappa_L} A \alpha_R, \quad (6a)$$

$$V_I = \frac{\Gamma^2}{4} \alpha_I^2. \quad (6b)$$

The potentials are harmonic, as expected for a linear cavity. The only difference between  $V_R$  and  $V_I$  is that the minimum of  $V_R$  is displaced from zero by the laser amplitude entering the cavity.

We can now describe the optical dynamics in terms of two decoupled OLEs involving scalar potentials:

$$\dot{\alpha}_{R,I} = -\frac{1}{\Gamma} \frac{\partial V_{R,I}}{\partial \alpha_{R,I}} + D \zeta_{R,I}(t). \quad (7)$$

Next we demonstrate that a resonantly driven linear cavity admits an effective equilibrium description. The effective temperature  $T$  is related to the noise variance  $D^2$  via the fluctuation-dissipation relation  $\Gamma D^2 = 2k_B T$ , with  $k_B$  the Boltzmann constant.

We numerically solved Eq. (1) with noise using the xSPDE MATLAB toolbox [59]. Based on the resultant

stochastic trajectories  $\alpha_R(t)$ , we calculated probability density functions (PDFs) for  $\alpha_R$ , namely,  $P(\alpha_R)$ . Figure 2(b) shows results for three different values of  $D/\sqrt{\Gamma}$  as curves of different color. All PDFs have negligible statistical error because they are based on trajectories lasting  $\Gamma t = 10^6$ , and  $\Gamma^{-1}$  is the relaxation time to a steady state. Figure 2(b) also shows, as white dashed curves, the corresponding equilibrium Boltzmann distributions

$$P(\alpha_R) = \mathcal{N} e^{-V_R/k_B T}, \quad (8)$$

with  $\mathcal{N}$  a normalization constant. These are first-principles calculations and not fits to the numerical data. We inserted the potential  $V_R$  from Eq. (6a) into Eq. (8) to calculate  $P(\alpha_R)$ , and used  $\Gamma D^2 = 2k_B T$  to determine the temperature  $T$ .  $V_I$  can be neglected because  $\alpha_I$  is decoupled from  $\alpha_R$ , and the driving field acts on  $\alpha_R$  only. While not shown here, we confirmed the accuracy of the fluctuation-dissipation relation by calculating  $P(\alpha_R)$  for different values of  $\Gamma$  and verifying its agreement with the Boltzmann distribution.

The preceding analysis demonstrates that a resonantly driven linear optical cavity is mathematically equivalent to thermodynamic systems described by OLEs. This equivalence establishes a connection between photonics and stochastic thermodynamics, where studies of OLEs have elucidated fundamental limits to the energetics and information processing capabilities of small material systems. Thus, many of those results can also serve to assess the energetic and information processing performance of noisy optical systems.

The effective temperature of the intracavity field is not constrained by the temperature of the medium in the cavity. In fact, even in an empty cavity, the effective temperature can be increased by imprinting white noise on the driving laser using modulators [34,35]; the case of colored noise is beyond the scope of this paper. The effective temperature, associated with optical noise, is also different from the temperature reached by electromagnetic radiation when it equilibrates through interactions with matter [23]. We propose that the effective temperature of stochastic light can be understood from the perspective of the kinetic theory of gases. From that perspective, the temperature of an ideal gas is related to the average kinetic energy of the particles. A higher temperature increases the probability of finding a particle away from its equilibrium position at zero temperature. Noise in the laser amplitude and phase does the same to the intracavity light field: It increases the probability of finding field amplitudes and phases away from the equilibrium value at zero noise.

In the remainder of this paper we focus on understanding whether and how a nonlinear cavity driven off resonance admits an effective equilibrium description in terms of a scalar potential. The case of a linear cavity driven off resonance is discussed in Appendix B.

### IV. APPROXIMATE GRADIENT FLOW FOR A JUDICIOUSLY DRIVEN NONLINEAR CAVITY

Next we investigate the second way in which  $\vec{\nabla} \times \vec{F} = 0$  and gradient flow behavior can be expected. To this end, we calculated  $\vec{\nabla} \times \vec{F}$  using the steady-state solutions to Eq. (1) obtained by setting  $\dot{\alpha} = 0$ . For this and all nonlinear calculations in this paper, we assume a weak single-photon

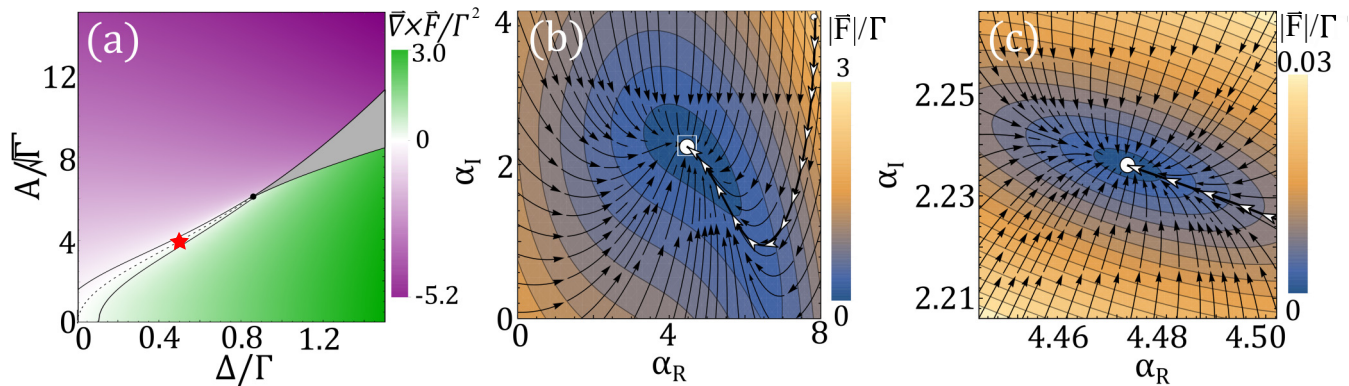


FIG. 3. (a) Curl of the deterministic force  $F$  versus the laser-cavity detuning  $\Delta$  and driving amplitude  $A$ , all referenced to the dissipation rate  $\Gamma$ . The black dot is where the steady-state solutions bifurcate, leading to bistability in the dark gray region. The black dashed curve indicates the path where  $|\vec{\nabla} \times \vec{F}| = 0$ . The light-colored region around the black dashed curve is where  $|\vec{\nabla} \times \vec{F}|/\Gamma^2 < 0.2$ , i.e., only a small nonconservative force is present. (b) Phase portrait for  $\Delta/\Gamma = 0.5$  and  $A/\sqrt{\Gamma} = 3.952$ . The driving parameters  $(\Delta/\Gamma, A/\sqrt{\Gamma})$ , indicated by the star in (a), are such that the steady-state intensity fulfills the zero-curl condition  $N = \Delta/2U$ . The black curve with white arrows follows the evolution of the intracavity field [obtained by solving Eq. (1)] when initialized at  $\alpha_R(0) = \alpha_I(0) = 7.9$ . (c) Zoom into the white square in (b). The white dot in (b) and (c) is the fixed point.

nonlinearity  $U/\Gamma = 0.01$ . This value is typical of state-of-the-art single-mode semiconductor cavities [60]. The exact value of  $U/\Gamma$  is not important. Nonlinearities emerge even for arbitrarily small  $U/\Gamma$ , provided that  $A$  is sufficiently large to make  $UN \gtrsim \Gamma$ . However,  $U \ll \Gamma$  is required to justify our description neglecting quantum effects. As shown by Vogel and Risken, only for  $U \ll \Gamma$  the state of the intracavity field is characterized by a positive Wigner function which can be interpreted as a classical probability distribution [19].

Figure 3(a) shows  $|\vec{\nabla} \times \vec{F}|/\Gamma^2$  in color as a function of  $\Delta/\Gamma$  and  $A/\sqrt{\Gamma}$ . Starting from weak on-resonance driving ( $A/\sqrt{\Gamma} \rightarrow 0, \Delta/\Gamma = 0$ ), Fig. 3(a) shows that increasing either  $A/\sqrt{\Gamma}$  or  $\Delta/\Gamma$  alone makes the curl of  $\vec{F}$  grow in magnitude. The resultant rotational force is illustrated in Fig. 10 of Appendix B for the particular case of  $U = 0$  and  $\Delta \neq 0$ . If  $\alpha$  is perturbed or initialized away from the fixed point, the rotational force makes  $\alpha$  descend to the fixed point along a spiral. This contrasts with the gradient descent observed in the previous section.

Interestingly, Fig. 3(a) shows that  $\vec{\nabla} \times \vec{F} = 0$  for certain off-resonance nonlinear conditions. In particular, there exists a path in parameter space ( $\Delta/\Gamma$  and  $A/\sqrt{\Gamma}$ ) along which the cavity can be driven from the vacuum state into the bistable regime while maintaining  $\vec{\nabla} \times \vec{F} = 0$  continuously; this path is shown as a dashed black curve in Fig. 3(a). In the conclusions we explain the relevance of this path to the solution of optimization problems using nonlinear optical cavities as proposed in Ref. [16].

Figure 3(b) shows the phase portrait of the system for  $\Delta/\Gamma = 0.5$  and  $A/\sqrt{\Gamma} = 3.952$  [at the star in Fig. 3(a)], where  $\vec{\nabla} \times \vec{F} = 0$ . The force field deviates from gradient flow. To emphasize this, in Fig. 3(b) we plot as a black curve with white arrows the evolution of the deterministic system initialized far from the fixed point. This curve was obtained by numerically solving Eq. (1) with  $D = 0$  and initial conditions  $\alpha_R(0) = \alpha_I(0) = 7.9$ . Far from the fixed point, the force vectors are neither perpendicular to the contours of constant

force magnitude nor are they pointing to the fixed point. However, this situation changes as the system approaches the fixed point. To show this effect more clearly, in Fig. 3(c) we present a zoomed-in view of Fig. 3(b). This view shows approximate gradient flow near the fixed point: The field descends to the fixed point along curves that are approximately perpendicular to the contours of constant force magnitude.

We can reconcile the results in Figs. 3(b) and 3(c) with those in Fig. 3(a) by recalling that  $\vec{\nabla} \times \vec{F}$  was evaluated using the steady-state solutions to Eq. (1), i.e., at the fixed points. Thus, the path in Fig. 3(a) where  $\vec{\nabla} \times \vec{F} = 0$  pertains only to the fixed points. Deviations from the fixed point change the intracavity intensity  $N$ , in turn modifying  $\vec{\nabla} \times \vec{F}$  according to Eq. (5). Such deviations are inevitable in the presence of noise. Consequently, an effective equilibrium description of light in a nonlinear cavity seems questionable even if the force (at the fixed point) is purely conservative.

## V. APPROXIMATE POTENTIAL FOR A NONLINEAR CAVITY

The previous section showed lack of gradient flow when the field in a nonlinear cavity driven off resonance is displaced from the fixed point. That result seems to preclude an effective equilibrium description in terms of a scalar potential. Nonetheless, we show next that an approximate effective equilibrium description in terms of a 1D scalar potential is still possible. However, the relevant potential is neither  $V_R$  nor  $V_I$ .

Let us first compare the cavity spectral response in the linear and nonlinear regimes, neglecting noise ( $D = 0$ ). The linear regime is accessed via weak driving. This results in an approximately Lorentzian resonance line shape, as the red curve in Fig. 4(a) shows. The nonlinear regime is accessed via strong driving. Since  $U > 0$ , the resonance line shape bends to the right and a region of bistability emerges. This is shown in Fig. 4(a), with green and gray curves representing stable and unstable states.

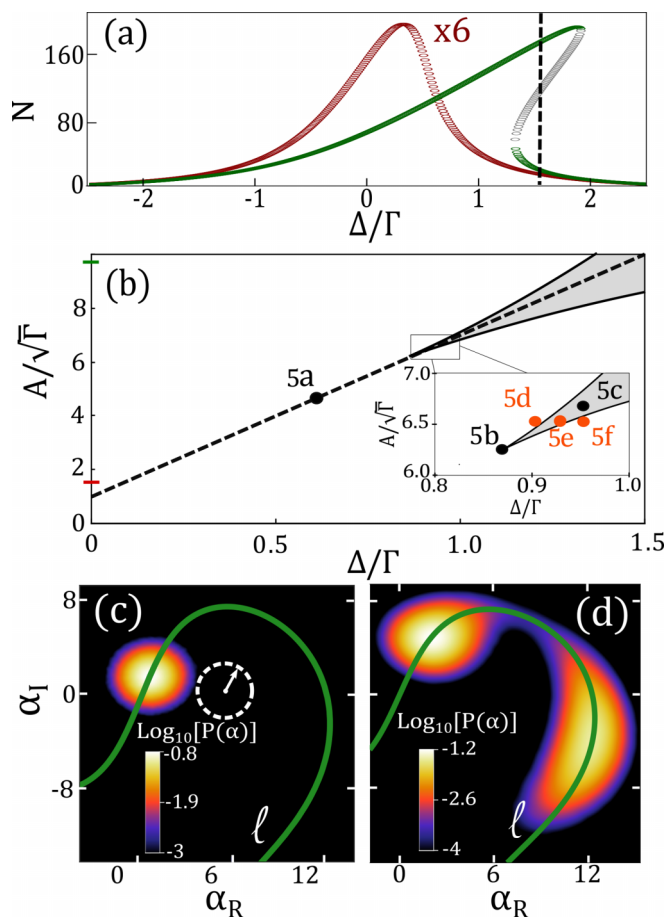


FIG. 4. (a) Number of photons,  $N$ , versus  $\Delta/\Gamma$  for two different driving amplitudes  $A$ .  $A/\sqrt{\Gamma} = 1.4$  for the red curve, where all states are stable.  $A/\sqrt{\Gamma} = 9.71$  for the green and gray curves, which correspond to stable and unstable states, respectively. The dashed line indicates the detuning considered in (d). (b) Number of stable steady states versus driving parameters in a Kerr-nonlinear cavity. White and gray areas correspond to one and two stable states, respectively. Entering the bistability along the dashed line corresponds to a supercritical pitchfork bifurcation. The inset zooms into the vicinity of the bifurcation, and indicates the driving conditions considered in Fig. 5. The green and red ticks on the vertical axis indicate the two driving amplitudes considered in (a). [(c), (d)] The PDF for the intracavity field obtained by numerically solving Eq. (1). The driving conditions are (c)  $A/\sqrt{\Gamma} = 1.4$  and  $\Delta/\Gamma = 0$ , (d)  $A/\sqrt{\Gamma} = 9.71$  and  $\Delta/\Gamma = 1.5$ . Green curves are the path  $\ell$  where  $\dot{\alpha}_I = 0$  and the potential  $V_{\text{app}}$  is defined. The dashed circle in (c) indicates the location of the PDF as predicted by Eqs. (6) and (8), in disagreement with numerical results.

Figure 4(b) shows regions where the cavity supports one and two stable steady states as white and gray areas, respectively. Figures 4(c) and 4(d) show PDFs for  $\alpha$  at two distinct driving conditions. These PDFs were calculated based on stochastic trajectories of  $\alpha(t)$ . We calculated eight trajectories with different noise realizations  $\zeta(t)$ , all with a large duration  $\Gamma t = 10^6$  and  $D = 2\sqrt{\Gamma}/2$ . With this amount of data, statistical errors in the calculated PDFs are negligible and undetectable in any of our plots. Figure 4(c) was obtained for  $A/\sqrt{\Gamma} = 1.4$  [corresponding to the red curve in Fig. 4(a)]

and  $\Delta/\Gamma = 0$ . The slightly larger uncertainty of the state along  $\alpha_R$  than along  $\alpha_I$  is a mild squeezing effect due to the nonlinearity. Figure 4(d) shows the PDF for  $A/\sqrt{\Gamma} = 9.71$  and  $\Delta/\Gamma = 1.5$ , which probes states at the intersections of the green curves and the dashed line in Fig. 4(a). The observed bimodal distribution indicates bistability.

In general, the dynamics of the 2D field  $\alpha$  cannot be fully described in terms of a 1D scalar potential. However, we hypothesize that, for  $\Omega \ll \Gamma$ , the dynamics of the undriven degree of freedom  $\alpha_I$  can be disregarded. In that case, an approximate 1D potential  $V_{\text{app}}$  may capture the essential dynamics of the full 2D system. To test this idea, we plot the values of  $(\alpha_R, \alpha_I)$  for which  $\dot{\alpha}_I = 0$  as green curves in Figs. 4(c) and 4(d). This one-dimensional path  $\ell$  physically corresponds to an electromagnetic field quadrature being static. This behavior can be measured using standard balanced homodyne detection methods [61]. Notice how the path  $\ell$  passes through the main features of the PDF even in the nonlinear regime of bistability. Remarkably,  $\ell$  closely follows the most probable path between the two attractors in Fig. 4(d). Based on this observation, we propose defining  $V_{\text{app}}$  along  $\ell$ . We stress that  $V_{\text{app}}$  is an entirely different potential from  $V_R$  and  $V_I$ , which are not centered along the path  $\ell$  and fail dramatically even in the monostable regime. For reference, the white dashed circle in Fig. 4(c) indicates the expected location of the peak in the PDF if one were to naively apply Eqs. (6) and (8) in this case.

Along the path  $\ell$ , the time evolution of  $\alpha_R$  acts as a local force approximately capturing the full system's dynamics:

$$F_{\text{app}} = \Gamma \dot{\alpha}_R \Big|_{\dot{\alpha}_I=0} = \Gamma \sqrt{\kappa_L} A - \frac{\Gamma^2}{2\alpha_R} (\alpha_R^2 + \alpha_I^2). \quad (9)$$

The approximate potential  $V_{\text{app}}$  is obtained by integrating  $F_{\text{app}}$  along  $\ell$ :

$$V_{\text{app}}(\alpha_R, \alpha_I) = - \int F_{\text{app}} d\ell. \quad (10)$$

We now want to relate positions along the path  $\ell$  to light intensities  $N$ . To this end, we recall that the distance of any point in the  $(\alpha_R, \alpha_I)$  plane from the origin is  $\sqrt{N} = \sqrt{\alpha_R^2 + \alpha_I^2}$ . Using this relation, in Fig. 5 we plot  $V_{\text{app}}(\sqrt{N})$  as red curves for different driving conditions. Figures 5(a)–5(c) are evaluated along the dashed line in Fig. 4(b), crossing the point  $\{\Delta_c, A_c\} = \{\Gamma\sqrt{3}/2, \Gamma^{3/2}3^{-3/4}/\sqrt{\kappa_L U}\}$  where the steady-state intensity bifurcates [14]; note that the dashed line in Fig. 4(b) is not the same as the dashed curve in Fig. 3(a). The observed transformation of  $V_{\text{app}}$  from single well to double well in Figs. 5(a)–5(c) corresponds to a system undergoing a supercritical pitchfork bifurcation. To demonstrate how  $V_{\text{app}}$  captures the distribution of the full system, the shaded areas in Fig. 5 show PDFs obtained from stochastic simulations of Eq. (1). Notice the good agreement between the peaks in the PDF and the dips in  $V_{\text{app}}$  for the various driving conditions.

Figures 5(d)–5(f) show that  $V_{\text{app}}$  approximately captures the distribution of light in the cavity also when  $\Delta/\Gamma$  is varied while  $A/\sqrt{\Gamma}$  is constant. In particular, we plot  $V_{\text{app}}$  at the driving conditions indicated by the orange dots in Fig. 4(b). Figures 5(d)–5(f) show how  $V_{\text{app}}$  tilts right to left as  $\Delta/\Gamma$  increases. Correspondingly, the numerically calculated

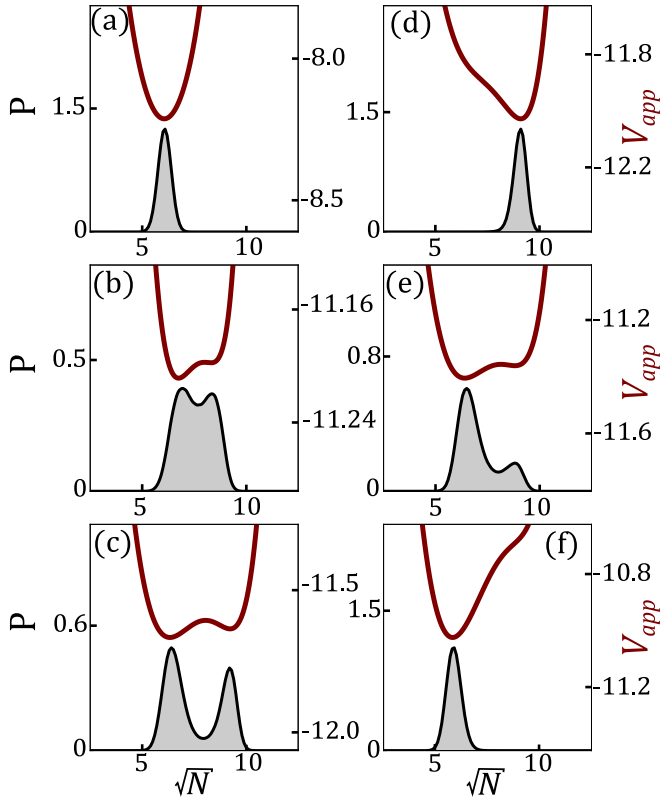


FIG. 5. Red curves are the approximate potential  $V_{\text{app}}$ . Shaded areas are PDFs for the field amplitude  $\sqrt{N}$ . [(a)–(c)] Driving conditions are along the dashed line in Fig. 4(b). The PDF and  $V_{\text{app}}$  are reshaped as  $A/\sqrt{\Gamma}$  and  $\Delta/\Gamma$  increase and the system undergoes a supercritical pitchfork bifurcation. [(d)–(f)] Driving conditions are indicated by the orange dots in Fig. 4(b). The PDF and  $V_{\text{app}}$  tilt due to a change in  $\Delta/\Gamma$ .

PDFs for the full system [Eq. (1)] show the same behavior. The success of  $V_{\text{app}}$  is remarkable considering that it is a 1D scalar potential used to describe a 2D nonconservative system. Moreover, this effective 1D equilibrium description works reasonably well even in the highly nonlinear regime of bistability where  $UN \sim \Gamma$ . A more quantitative analysis is presented in the next section.

## VI. DEVIATIONS FROM BOLTZMANN STATISTICS

In this section we assess the accuracy of  $V_{\text{app}}$  by comparing probability distributions of field amplitudes  $P(\sqrt{N})$  calculated in two different ways. First we calculate  $P(\sqrt{N})$  for the full system along the path  $\ell$ . We call those distributions  $P_{\text{full}}(\sqrt{N})$ . We obtained  $P_{\text{full}}(\sqrt{N})$  by numerically solving Eq. (1) with  $U/\Gamma = 0.01$  and  $D = \sqrt{\Gamma}/2/2$ . We evolved the system for a time  $\Gamma t = 10^5$  and ran simulations for 120 different noise realizations. The resultant  $P_{\text{full}}(\sqrt{N})$  are shown in Fig. 6 as areas of different color for six different driving conditions  $(A/\sqrt{\Gamma}, \Delta/\Gamma)$ . All driving conditions lie along the dashed line in the figure inset, which is the same dashed line shown in Fig. 4(b). Here, again, we verified that statistical errors in all PDFs are much smaller than the thickness of the plotted curves. Next we calculate equilibrium Boltzmann

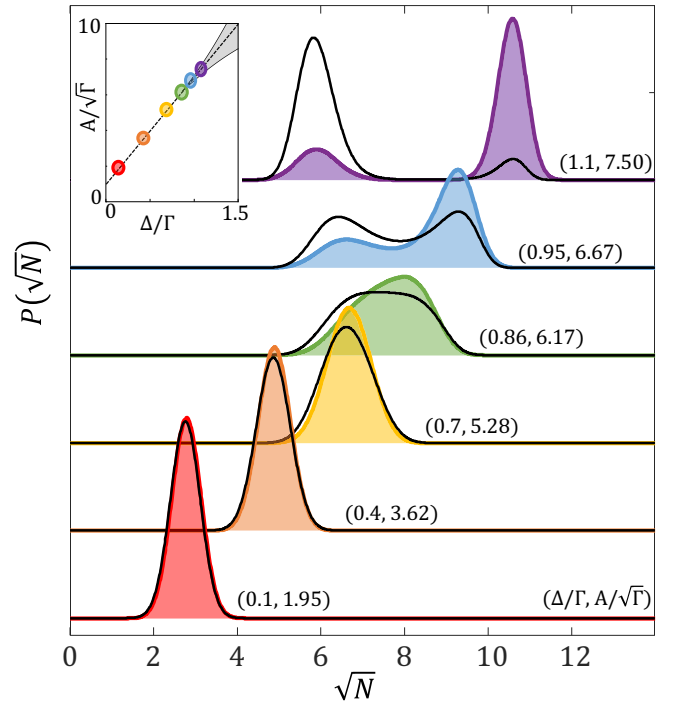


FIG. 6. PDF of the field amplitude  $\sqrt{N}$  for six values of the driving amplitude  $A/\sqrt{\Gamma}$  and the detuning  $\Delta/\Gamma$ , referenced to the dissipation  $\Gamma$ .  $D = \sqrt{\Gamma}/2/2$  in all calculations. Colored areas are obtained by solving Eq. (1). Black curves are Boltzmann distributions for the potential  $V_{\text{app}}$ . Inset: Number of stable steady states versus driving parameters in a Kerr-nonlinear cavity, with colored dots indicating the values of  $A/\sqrt{\Gamma}$  and  $\Delta/\Gamma$  considered in the main panel.

distributions by inserting  $V_{\text{app}}$  and the effective temperature  $T = \Gamma D^2/2k_B$  in Eq. (8). The Boltzmann distributions, which we call  $P_{\text{Bol}}(\sqrt{N})$ , are the black curves over  $P_{\text{full}}(\sqrt{N})$  in Fig. 6.

For small  $A/\sqrt{\Gamma}$  and  $\Delta/\Gamma$ ,  $P_{\text{full}}(\sqrt{N})$  and  $P_{\text{Bol}}(\sqrt{N})$  are in very good agreement. This is expected based on the results in Fig. 2(b). Then, as  $A/\sqrt{\Gamma}$  and  $\Delta/\Gamma$  increase,  $P_{\text{full}}(\sqrt{N})$  increasingly deviates from  $P_{\text{Bol}}(\sqrt{N})$ . We quantify the difference between the two distributions via the overlap integral

$$\epsilon = \frac{1}{2} \int |P_{\text{full}} - P_{\text{Bol}}| d\sqrt{N}. \quad (11)$$

$\epsilon = 0$  when  $P_{\text{full}}(\sqrt{N}) = P_{\text{Bol}}(\sqrt{N})$ , and  $\epsilon = 1$  when the two distributions have zero overlap.

Figure 7(a) shows that  $\epsilon$  is a nonmonotonic function of the distance to the bifurcation, controlled via  $A/\sqrt{\Gamma}$  and  $\Delta/\Gamma$ . A large  $\epsilon$  is presumably the result of a nonconservative force, which is absent in the Boltzmann distribution taking into account  $V_{\text{app}}$  only. We tested this hypothesis by calculating two quantities which are related but not exactly the same. First we calculated the ratio  $4|\Omega|^2/\Gamma^2$ , which is the coupling strength between  $\alpha_R$  and  $\alpha_I$  relative to the dissipation. Since  $\alpha_R$  and  $\alpha_I$  each experience a purely conservative force proportional to  $\Gamma^2/2$  for  $\Omega = 0$ , the quantity  $4|\Omega|^2/\Gamma^2$  is related to the ratio of

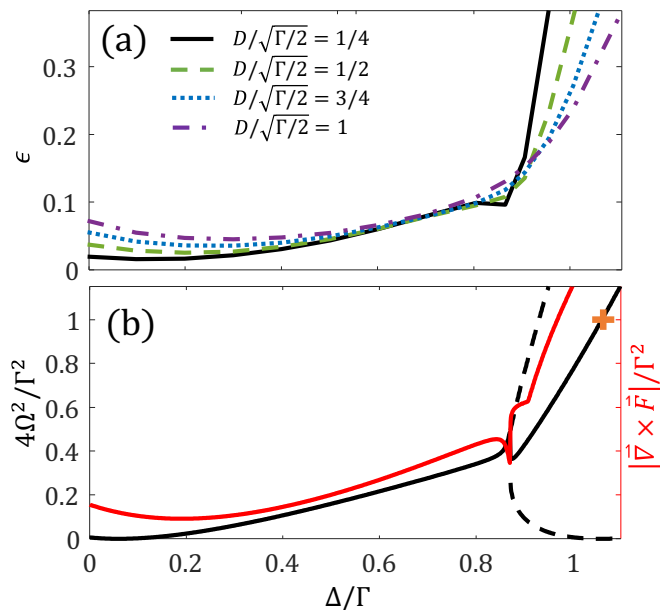


FIG. 7. (a) Deviation  $\epsilon$  from the Boltzmann distribution, as defined by Eq. (11), for the same values of  $A/\sqrt{\Gamma}$  and  $\Delta/\Gamma$  considered in Fig. 6, and for various  $D$ . (b) Black curves correspond to the ratio of off-diagonal to diagonal parts of the first matrix in the right-hand side of Eq. (2). This ratio quantifies the mutual coupling between the field components  $\alpha_R$  and  $\alpha_I$ . In the regime of bistability, each dashed black curve corresponds to one of the two stable states, and the solid black curve is their mean. The orange cross marks the boundary between weak and strong coupling between  $\alpha_R$  and  $\alpha_I$ . The red curve corresponds to the magnitude of the curl of the force (referenced to  $\Gamma$ ) as indicated on the right axis.

nonconservative to conservative forces in the 2D system. The second quantity we calculated is  $|\vec{\nabla} \times \vec{F}|/\Gamma^2$  using the steady-state solutions, like we did in Fig. 3(a). Both quantities were calculated for driving conditions along the identical dashed lines in Figs. 4(b) and 6.

Figure 7(b) shows  $4|\Omega|^2/\Gamma^2$  as a black curve, and  $|\vec{\nabla} \times \vec{F}|/\Gamma^2$  as a red curve. Both quantities are unique in the monostable regime, but double valued in the bistable regime of  $\Delta/\Gamma > \sqrt{3}/2 \approx 0.87$ . Since the distributions  $P_{\text{full}}(\sqrt{N})$  in the bistability result from dynamics involving two states with different  $N$ , we focus on average quantities. We illustrate the relation between average and state-dependent quantities in Fig. 7(b) by plotting the values of  $4|\Omega|^2/\Gamma^2$  for each state in the bistability as dashed black curves, and their average as a solid black curve. For brevity, we only plot the average  $|\vec{\nabla} \times \vec{F}|/\Gamma^2$  as a red curve.

Overall, Fig. 7(b) shows that  $4|\Omega|^2/\Gamma^2$  and  $|\vec{\nabla} \times \vec{F}|/\Gamma^2$  depend on  $\Delta/\Gamma$  in a similar way as  $\epsilon$  does. This indicates that deviations from the equilibrium Boltzmann distribution are indeed associated with the nonconservative force. Differences between  $4|\Omega|^2/\Gamma^2$  and  $|\vec{\nabla} \times \vec{F}|/\Gamma^2$  follow from the fact that the nonconservative force arises from a nonvanishing coupling  $\Omega$  between  $\alpha_R$  and  $\alpha_I$ , but the curl of  $F$  is not fully determined by  $\Omega$ . This can be recognized by rewriting Eq. (5) as  $|\vec{\nabla} \times \vec{F}|/\Gamma = |2\Delta - 4UN| = |-2\Omega - 2UN|$ . The extra  $-2UN$  term, which depends on the driving strength in

a nonlinear way, results in differences between red and black curves in Fig. 7(b).

Next we assess whether the noise strength affects  $\epsilon$ , and hence the accuracy of our effective equilibrium description. In Fig. 7(a) we plot  $\epsilon$  as a function of  $\Delta/\Gamma$  for four different  $D$ . For small  $\Delta/\Gamma$ ,  $\epsilon$  increases with  $D$ . This is expected since noise drives the system away from the path  $\ell$  on which  $V_{\text{app}}$  is defined. Interestingly, however,  $\epsilon$  decreases with  $D$  for  $\Delta/\Gamma \gtrsim 0.9$ . The stochastic force suppresses the effects of the nonconservative force in this regime, and the accuracy of our effective equilibrium description in terms of  $V_{\text{app}}$  improves. In the next section we offer an explanation for this effect in view of the phase portrait of the system.

While  $P_{\text{full}}(\sqrt{N})$  strongly deviates from  $P_{\text{Bol}}(\sqrt{N})$  deep in the bistable regime, the deviation is quite small close to the bifurcation at  $\Delta/\Gamma = \sqrt{3}/2 \approx 0.87$ . Notice in Fig. 7(a) that  $\epsilon \approx 0.1$  around  $\Delta/\Gamma = 0.9$ . The small ( $\sim 10\%$ ) deviation from equilibrium behavior justifies our claim that  $V_{\text{app}}$  approximately captures the full system's dynamics. This is an important result because most of the interesting physics occurs near the bifurcation.

## VII. EXCEPTIONAL-LIKE POINT FOR THE FLUCTUATIONS

Here we pursue an understanding of the physics underlying the limited validity range of the scalar potential  $V_{\text{app}}$ . To this end, we analyze the spectrum of small fluctuations on top of the steady state. We perform a standard linear stability analysis as discussed in Refs. [39,52], for example. Planar cavities admit qualitatively similar stability analyses [62].

Consider the effect of adding a small fluctuation  $\delta\alpha = \delta\alpha_R + i\delta\alpha_I$  to the light field, i.e., let  $\alpha \rightarrow \alpha + \delta\alpha$  in Eq. (1). By only retaining terms that are linear in  $\delta\alpha$ , we get the following equation of motion for the fluctuations:

$$\begin{pmatrix} \delta\dot{\alpha}_R \\ \delta\dot{\alpha}_I \end{pmatrix} = \begin{pmatrix} -\frac{\Gamma}{2} + 2U\alpha_R\alpha_I & U(\alpha_R^2 + 3\alpha_I^2) - \Delta \\ \Delta - U(3\alpha_R^2 + \alpha_I^2) & -\frac{\Gamma}{2} - 2U\alpha_R\alpha_I \end{pmatrix} \begin{pmatrix} \delta\alpha_R \\ \delta\alpha_I \end{pmatrix}. \quad (12)$$

Equation (12) has solutions of the form

$$\vec{\delta\alpha} = \vec{\eta} e^{\lambda t}, \quad (13)$$

where  $\vec{\eta}$  are the eigenvectors and  $\lambda$  the eigenvalues of the  $2 \times 2$  matrix in Eq. (12). The eigenvalues

$$\lambda_{\pm} = -\Gamma/2 \pm \sqrt{G(U, \Delta, N)} \quad (14)$$

comprise the spectrum of the fluctuations. The function  $G = -(\Delta - UN)(\Delta - 3UN)$  determines the stability of the fixed points, and the validity range of the potential  $V_{\text{app}}$  as explained next.

Figure 8 illustrates how the force exerted on  $\alpha$  depends on the sign of  $G$ . Figures 8(a) and 8(b) correspond to positive and negative  $G$ , respectively. Figure 8(a) was obtained for  $A/\sqrt{\Gamma} = 6.95$  and  $\Delta/\Gamma = 1$ , which places the cavity within the bistability regime and close to the point where the steady-state intensity  $N$  bifurcates [see Fig. 4(b) or Fig. 6]. Stable and unstable fixed points are represented by white and red dots, respectively. The unstable fixed point has purely real eigenvalues with opposite sign, and it is therefore a saddle.

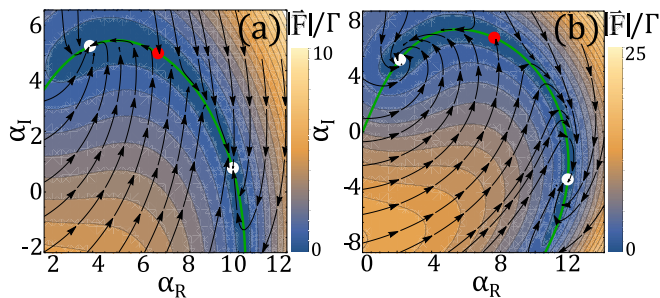


FIG. 8. [(a), (b)] Phase portrait of the Kerr-nonlinear cavity evaluated at the driving amplitudes and detunings indicated in Fig. 9(a). Color and arrows represent the force magnitude and direction, respectively. White dots are stable fixed points, and red dots are unstable fixed points. Green curves indicate the path  $\ell$  where  $\dot{\alpha}_I = 0$  and the potential  $V_{\text{app}}$  is defined.  $V_{\text{app}}$  works well in (a) where there is approximate gradient flow, but not in (b) where nonconservative forces dominate and lead to spiraling orbits around the stable fixed points.

The green curve is the path  $\ell$  (where  $\dot{\alpha}_I = 0$ ) along which we evaluated  $V_{\text{app}}$ . Notice how all force vectors point to the path  $\ell$ , which connects the unstable and stable fixed points. If  $\alpha$  is displaced from  $\ell$  by the stochastic force, the deterministic force ensures its return to  $\ell$ . This results in approximate gradient flow in one dimension, thereby explaining why  $V_{\text{app}}$  approximately captures the full system’s dynamics close to the bifurcation. We can also understand this behavior based on the spectrum of fluctuations. For driving conditions giving  $G > 0$ , the eigenvalues  $\lambda_{\pm}$  turn out to be real negative numbers. This results in overdamped fluctuations, stable fixed points which are sinks, and approximate 1D gradient flow.

The physics is different for  $G < 0$ . For example, Fig. 8(b) shows the phase portrait for  $A/\sqrt{\Gamma} = 9$  and  $\Delta/\Gamma = 1.38$ , which places the cavity within the bistability regime but further away from the bifurcation. The change in driving conditions has transformed the stable sinks into stable foci. Each stable focus has a spiraling force field around it, implying that a fluctuation in one field component ( $\alpha_R$  or  $\alpha_I$ ) couples to the other component. When this coupling is strong, the non-conservative force dominates, the fluctuations are no longer overdamped, and any perturbation causes the field to stabilize at a new orbit in the two-dimensional force field. Clearly, a 1D scalar potential cannot fully capture the system’s dynamics in this regime.

Figure 8(b) also reveals why increasing the noise strength effectively suppresses the effects of the nonconservative force deep in the bistable regime. The spiraling orbits near the stable fixed points in Fig. 8(b) are due to the nonconservative force. When the standard deviation of the noise is small,  $\alpha$  mainly explores those spiraling orbits which are not contained in our effective 1D potential  $V_{\text{app}}$ . In contrast, when the standard deviation of the noise is large,  $\alpha$  switches between the stable fixed points more often. In doing so,  $\alpha$  mainly passes through the path  $\ell$  along which  $V_{\text{app}}$  is defined. Hence, for larger standard deviation of the noise the dynamics more closely resembles Brownian motion in a 1D scalar potential defined along  $\ell$ .

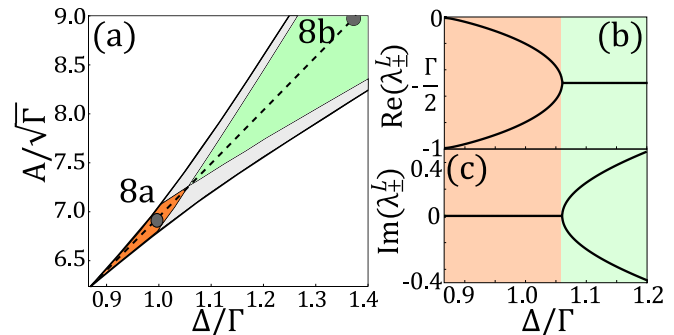


FIG. 9. (a) Classification of steady-state regimes as in Fig. 4(b), but for a reduced range of driving amplitude  $A$  and detuning  $\Delta$  both referenced to the dissipation  $\Gamma$ . The orange region close to the bifurcation is where the eigenvalues  $\lambda_{\pm}$  in Eq. (14) are purely real, the field components  $\alpha_R$  and  $\alpha_I$  are weakly coupled, and there is a saddle-sink connection between the fixed points. This is the region where  $V_{\text{app}}$  works well. The green region is where both eigenvalues of both states have a nonzero imaginary part. In the gray region, one of the two states has eigenvalues with nonzero imaginary part.  $V_{\text{app}}$  fails to properly capture system’s dynamics in the gray and green regions. (b) Real and (c) imaginary parts of the eigenvalues of the low-density state along the dashed line in (a). Orange and green regions have the same meaning as in (a). Real and imaginary parts of the eigenvalues coalesce at  $\Delta/\Gamma = 1.06$ , which resembles an exceptional point.

We can further elucidate the above effects by considering the spectrum of fluctuations. For this purpose, we calculated the eigenvalues  $\lambda_{\pm}$  in Eq. (14) in the bistable regime. Based on the results, we distinguish three regimes indicated by areas of different color in Fig. 9(a). In the orange region, all eigenvalues  $\lambda_{\pm}$  are purely real and negative for both states. Consequently, the fluctuations are overdamped and there is a saddle-sink connection between the fixed points. In that regime,  $\ell$  (defined by  $\dot{\alpha}_I = 0$ ) closely follows the most probable path between the stable fixed points, and the dynamics is approximately captured by  $V_{\text{app}}$  defined along  $\ell$ . In contrast,  $V_{\text{app}}$  fails to capture the full system’s dynamics in the gray and the green regions. This is due to the fact that the eigenvalues are imaginary (oscillating fluctuations) for one of the steady states in the gray regions, and for both states in the green region.

In Figs. 9(b) and 9(c) we plot the real and imaginary parts of  $\lambda_{\pm}$ , respectively, for the low-photon-density bistable state. We plot the eigenvalues as a function of  $\Delta/\Gamma$  while also varying  $A/\sqrt{\Gamma}$ , thereby keeping the system along the dashed line in Fig. 6. The fluctuations are overdamped and effectively decoupled in the orange region, and oscillatory and strongly coupled in the green region. Interestingly, real and imaginary parts of both eigenvalues coalesce at the boundary of these two regions. To the left (right) side of this coalescence point, the real (imaginary) parts of  $\lambda$  split while the imaginary (real) parts cross. This is the typical behavior of the eigenvalues of a non-Hermitian Hamiltonian describing two linearly coupled linear modes [63–67]. Thus, the degeneracy point at  $\Delta/\Gamma = 1.06$  resembles an exceptional point for the fluctuations.

The exceptional-like point for the fluctuations separates the regimes in which a bistable cavity can or cannot be approximately described by the potential  $V_{\text{app}}$ . This is an interesting



analogy to the non-Hermitian physics of coupled modes. There, the exceptional point defines the boundary between weak and strong coupling between the two modes [65]. The similarity is even more striking when we consider that the mutual coupling between field components  $\alpha_{R,I}$  transitions from weak to strong at  $\Delta/\Gamma = 1.06$ . Indeed, for  $\Delta/\Gamma = 1.06$  we have  $4|\Omega|^2 \approx \Gamma^2$ , which corresponds to the boundary between weak and strong coupling between the field components  $\alpha_{R,I}$ . The point  $4|\Omega|^2 = \Gamma^2$  is indicated by an orange cross in Fig. 7(b). The large values of  $\epsilon$  around and above this point in Fig. 7(b) indicate that large deviations from equilibrium behavior are indeed related to a qualitative change in the fluctuation spectrum occurring at an exceptional-like point.

In two-mode systems described by a non-Hermitian Hamiltonian, the exceptional point (EP) also corresponds to a parity-time ( $\mathcal{PT}$ )-symmetry-breaking point [66]. On one side of the EP, the Hamiltonian is  $\mathcal{PT}$  symmetric and its eigenvalues are real. On the other side,  $\mathcal{PT}$  symmetry is broken and the eigenvalues are complex. A similar situation arises here, with the crucial difference that the relevant eigenvalues are of the  $2 \times 2$  Jacobian matrix in Eq. (12) instead of the Hamiltonian. This points to an interesting relation between the symmetry properties of the Jacobian and the accuracy of our effective 1D description in capturing the behavior of the full 2D system.

The preceding analysis elucidates the physics underlying the limited validity range of  $V_{\text{app}}$ . In particular, the maximum values of  $A/\sqrt{\Gamma}$  and  $\Delta/\Gamma$  for which  $V_{\text{app}}$  remains valid coincide with an exceptional-like point in the spectrum of small fluctuations on top of the steady-state field. On one side of the exceptional-like point, the light field experiences approximate gradient flow towards our 1D path  $\ell$  along which  $V_{\text{app}}$  is defined; an effective equilibrium description is valid in that case. On the other side of the exceptional-like point, the dynamics span the full 2D phase space and an effective equilibrium description in terms of  $V_{\text{app}}$  fails. The exceptional-like point for the fluctuations also coincides with the transition from weak to strong coupling between the field components  $\alpha_{R,I}$ . Our results establish interesting connections between the statistical physics of light in a single-mode nonlinear cavity, the non-Hermitian physics of its fluctuations, and the physics of strong versus weak coupling of degrees of freedom. A perspective arising from identifying these connections is provided in the next section.

### VIII. CONCLUSIONS AND PERSPECTIVES

To summarize, we first showed that stochastic light in a coherently driven nonlinear optical cavity is mathematically equivalent to two-dimensional overdamped Langevin dynamics with a nonconservative force. Only for a linear cavity driven on resonance there is an exact correspondence to Brownian motion in a scalar potential: The dissipation and driving amplitude exactly define the scalar potential, the noise variance and dissipation define an effective temperature, and the distribution of light in the cavity follows the equilibrium Boltzmann distribution. We then showed that the physics is more subtle when the cavity is nonlinear and driven off resonance. While an exact potential cannot be defined, we identified a path  $\ell$  along which the 1D scalar potential

$V_{\text{app}}$  captures the physics of the 2D system to a very good approximation. An effective equilibrium description of light in terms of  $V_{\text{app}}$  is possible even in the highly nonlinear and off-resonance regime of bistability. The accuracy of this description was shown to be a nonmonotonic function of the driving amplitude and frequency. Finally, we connected the effective equilibrium versus nonequilibrium behavior of the intracavity field with non-Hermitian physics of its fluctuations. The fluctuation spectrum exhibits an exceptional-like point at the boundary of the validity range of  $V_{\text{app}}$ .

Our results provide a detailed answer to a fundamental and long-standing question in resonant optics: Can a single noisy electromagnetic mode be understood in terms of Brownian motion within a scalar potential? While single-mode cavities have been studied and realized for decades, the question we addressed has recently acquired increased relevance. For example, many recent developments in the field of stochastic thermodynamics [25–27] involve overdamped Langevin dynamics. Important results about fluctuations of thermodynamic quantities, the efficiency of stochastic engines, and the precision of information-processing systems have emerged from understanding overdamped Langevin dynamics [24,26,27,68,69]. Our work establishes an important connection to that field. Single-mode cavities could be ideal systems for fundamental experiments in stochastic thermodynamics. One reason for this is the huge bandwidth easily accessible with optical systems. For instance, using a typical single-mode optical cavity with  $\Gamma^{-1} = 1$  ps, one could measure dynamics spanning 12 orders of magnitude in time within a second [5,8,34,35,57]; the dynamic range would be only limited by the memory of the electronics. One could therefore acquire great statistics about negative entropy production events, and probe fluctuation theorems with unprecedented accuracy, using mature optical technologies. Importantly, the ratio of conservative to nonconservative forces could be easily tuned by varying the laser power or frequency, thereby opening new perspectives. Beyond this fundamental physics perspective, a description of single-mode cavities in thermodynamic terms also offers intriguing technological perspectives. For instance, the framework of stochastic thermodynamics could be used to understand and optimize resonant optical technologies, like sensors, switches, memories, and other devices driven by noisy lasers. To that end, thermodynamic quantities like heat and work would still need to be defined. The consistency of those definitions with the first and second laws of thermodynamics would also need to be verified. We foresee exciting discoveries in that direction, partly enabled by the ability to understand resonant optical systems in terms of Langevin dynamics within a potential.

Our results are also relevant in the context of optimization problems [16]. Recently, Kyriienko *et al.* numerically demonstrated that nonlinear cavity arrays can be used to solve  $NP$ -hard optimization problems in an all-optical way; the problem of interest is encoded in the intercavity couplings. If the total deterministic force exerted on the cavity fields (analogous to the force  $F$  in the single-cavity we studied) were purely conservative, the performance of Kyriienko's optimizer could be explained in terms of gradient descent [70]. Indeed, Leleu *et al.* explicitly showed that an array of overdamped Langevin oscillators with cubic nonlinearity driven across a

bifurcation solves an optimization problem encoded in the interoscillator couplings. However, Leleu's argument only holds for a purely conservative force which can be derived from a scalar potential. In contrast, the optimizers of Kyriienko *et al.* involve nonconservative forces. In this context, our results offer a plausible explanation for the surprisingly high success probabilities Kyriienko *et al.* found for their optimizer: While the nonconservative force of optical cavity arrays is strictly nonzero, its magnitude may be small. We furthermore suspect that, as for the single-cavity case, the full dynamics of each cavity in its 2D phase space might be captured by an effective 1D approximate potential. For the optimizer to succeed, effective equilibrium behavior (i.e., gradient flow) is mainly needed near the bifurcation, which is again similar to what we have observed for a single cavity in this article. While these speculations remain to be checked, our findings suggest that (approximate) gradient descent may be the mechanism underlying the surprisingly successful performance of cavity array optimizers.

### ACKNOWLEDGMENTS

This work is part of the research programme of the Netherlands Organisation for Scientific Research (NWO). We thank Nicola Carlon Zambon, Christopher Jarzynski, Sergio Ciliberto, Pieter Rein ten Wolde, and Martin van Hecke for stimulating discussions. S.R.K.R. acknowledges an ERC Starting Grant with Project No. 85269.

K.J.H.P. and J.B. contributed equally to this work.

### APPENDIX A: ASSUMPTIONS AND APPROXIMATIONS UNDERLYING OUR SINGLE-MODE MODEL

Equation (1) is valid when a single mode is well isolated, spectrally and spatially, from all other modes in the cavity. Otherwise, spatial patterns can arise due to the nonlinearity [62]. A mode can be isolated through strong three-dimensional optical confinement within a high-finesse cavity. Confinement along the optical axis is trivially accomplished by high-reflectivity mirrors. Lateral confinement can be achieved by using a micron-scale concave mirror [71,72], etching a micropillar out of a planar cavity [73], or making mesas within a planar cavity [74]. Results of numerous experiments with such microcavities are extremely well reproduced using single-mode descriptions [5,8,34,35,57,58].

One can arrive at our model, Eq. (1), starting from a quantum description by making the truncated Wigner approximation (TWA) [75]. Like in the mean-field approximation, in the TWA boson operators  $\hat{a}$  and  $\hat{a}^\dagger$  are replaced by their mean values:  $\hat{a} \rightarrow \langle \hat{a} \rangle = \alpha$  and  $\hat{a}^\dagger \rightarrow \langle \hat{a}^\dagger \rangle = \alpha^*$ . The TWA goes beyond a mean-field description by accounting for fluctuations via the classical noise terms  $\zeta_{R,I}$ .

The TWA is accurate when the single-photon nonlinearity is weak:  $U \ll \Gamma$ . Consequently, the mean intracavity photon number  $N = |\alpha|^2$  should largely exceed one in the bistable regime. While several recent works made progress towards realizing single-mode cavities with  $U \sim \Gamma$  [32,33,76,77], most optical cavities still operate in the  $U \ll \Gamma$  regime. The accuracy of the TWA in this regime has been verified many times, through quantitative agreement with experiments and

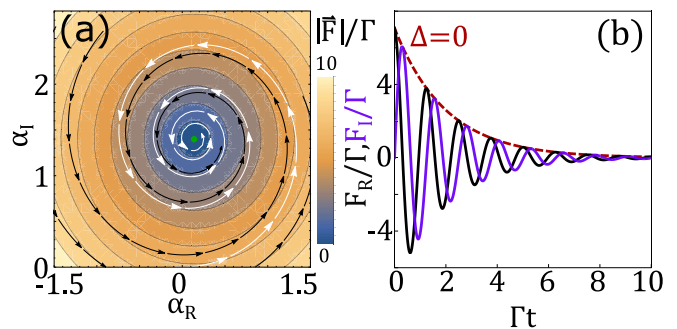


FIG. 10. (a) Phase portrait of a linear cavity driven off resonance with  $\Delta/\Gamma = 5$  and  $A/\sqrt{\Gamma} = 10$ . (b) Time evolution of the forces  $F_R$  and  $F_I$  acting on the real and imaginary parts of the field, namely,  $\alpha_R$  and  $\alpha_I$ , respectively. The dashed red curve is the evolution of  $F_R$  in a linear cavity driven on resonance, i.e.,  $\Delta = 0$ .

full quantum calculations [75]. For our system, PDFs calculated from the quantum master equation or the corresponding Fokker-Planck equation exactly match those calculated from sufficiently many and long solutions to the Langevin-type equation obtained via the TWA [Eq. (1)], provided  $U \ll \Gamma$  [19].

As explained in the main text, the stochastic terms  $\zeta_R$  and  $\zeta_I$  are mutually uncorrelated and each is  $\delta$  correlated. Moreover,  $\zeta_R$  and  $\zeta_I$  are multiplied by the same constant  $D$  such that both  $D\zeta_R$  and  $D\zeta_I$  have standard deviation  $D$ . In this way, using one pair of stochastic terms we account for two noise sources expected to influence any coherently driven cavity. One source of noise is fluctuations in the driving laser amplitude and phase. Since the coherent state of a laser is characterized by a symmetric two-dimensional Gaussian distribution in phase space, the stochastic terms  $D\zeta_R$  and  $D\zeta_I$  need to be uncorrelated and have equal variance to account for noise in the driving laser. The second source of noise we account for is fluctuations in the intracavity field due to its interaction with a memoryless environment. As usual, we assume that these fluctuations are random in phase. This demands, once again, for the stochastic terms to be uncorrelated and have equal variance. While one could describe the laser noise and the dissipation-induced noise using two distinct pairs of stochastic terms, for simplicity we can use only one pair because all noises are additive, Gaussian, white, and mutually uncorrelated. The noises are white, meaning  $\zeta_{R,I}$  are each  $\delta$  correlated, because of the Markov approximation. This corresponds to an instantaneous system-environment interaction. The Markov approximation holds for both the driving laser and the cavity it drives, which is our system of interest. Finally, we note that laser shot noise and cavity dissipation set a lower bound for the noise variance  $D^2$  [75]. However, more noise can be intrinsically present or added in experiments [34,35].

### APPENDIX B: LINEAR CAVITY DRIVEN OFF RESONANCE

Figure 10 illustrates the physics of a linear cavity driven far off resonance, with  $\Delta/\Gamma = 5$ . Since  $U = 0$  and  $\Delta/\Gamma$  is large,  $|\vec{\nabla} \times \vec{F}|/\Gamma^2$  is also large and the nonconservative force dominates the dynamics. Hence, the phase portrait of the

system, shown in Fig. 10(a), displays spiraling force vectors as expected for a rotational force field. This spiraling behavior precludes a description in terms of a scalar potential. Next, Fig. 10(b) illustrates the dynamics when  $\alpha$  is initialized far from the fixed point. Black and purple curves represent the forces  $F_R$  and  $F_I$ , which act on  $\alpha_R$  and  $\alpha_I$ , respectively. For reference, the dashed red curve shows the evolution of  $F_R$  for a linear cavity driven on resonance. Notice how the envelopes of  $F_R$  and  $F_I$  in the off-resonance case decay at the same rate as

$F_R$  in the on-resonance case. However, while for on-resonance driving the force decays exponentially (as expected for a gradient flow system), for off-resonance driving the forces decay in an oscillatory fashion. The oscillations imply energy exchange between  $\alpha_R$  and  $\alpha_I$ , as expected for two strongly coupled oscillators. Overall, Fig. 10 elucidates the relation between nonconservative dynamics and strong coupling between oscillators. This was already suggested in Fig. 7, but the absence of nonlinearity in Fig. 10 further clarifies the relation.

- 
- [1] R. Graham and H. Haken, Laserlight—first example of a second-order phase transition far away from thermal equilibrium, *Z. Phys.* **237**, 31 (1970).
- [2] H. Haken, Generalized Ginzburg-Landau equations for phase transition-like phenomena in lasers, nonlinear optics, hydrodynamics and chemical reactions, *Z. Phys.* **21**, 105 (1975).
- [3] M. Fitzpatrick, N. M. Sundaresan, A. C. Y. Li, J. Koch, and A. A. Houck, Observation of a Dissipative Phase Transition in a One-Dimensional Circuit QED Lattice, *Phys. Rev. X* **7**, 011016 (2017).
- [4] J. M. Fink, A. Dombi, A. Vukics, A. Wallraff, and P. Domokos, Observation of the Photon-Blockade Breakdown Phase Transition, *Phys. Rev. X* **7**, 011012 (2017).
- [5] S. R. K. Rodriguez, W. Casteels, F. Storme, N. Carlon Zambon, I. Sagnes, L. Le Gratiet, E. Galopin, A. Lemaître, A. Amo, C. Ciuti, and J. Bloch, Probing a Dissipative Phase Transition via Dynamical Optical Hysteresis, *Phys. Rev. Lett.* **118**, 247402 (2017).
- [6] W. Casteels, R. Fazio, and C. Ciuti, Critical dynamical properties of a first-order dissipative phase transition, *Phys. Rev. A* **95**, 012128 (2017).
- [7] M. Biondi, G. Blatter, H. E. Türeci, and S. Schmidt, Nonequilibrium gas-liquid transition in the driven-dissipative photonic lattice, *Phys. Rev. A* **96**, 043809 (2017).
- [8] T. Fink, A. Schade, S. Höfling, C. Schneider, and A. Imamoglu, Signatures of a dissipative phase transition in photon correlation measurements, *Nat. Phys.* **14**, 365 (2018).
- [9] J. T. Young, A. V. Gorshkov, M. Foss-Feig, and M. F. Maghrebi, Nonequilibrium Fixed Points of Coupled Ising Models, *Phys. Rev. X* **10**, 011039 (2020).
- [10] M. J. Hartmann, Quantum simulation with interacting photons, *J. Opt.* **18**, 104005 (2016).
- [11] J. J. Mendoza-Arenas, S. R. Clark, S. Felicetti, G. Romero, E. Solano, D. G. Angelakis, and D. Jaksch, Beyond mean-field bistability in driven-dissipative lattices: Bunching-antibunching transition and quantum simulation, *Phys. Rev. A* **93**, 023821 (2016).
- [12] C. Noh and D. G. Angelakis, Quantum simulations and many-body physics with light, *Rep. Prog. Phys.* **80**, 016401 (2016).
- [13] T. L. Heugel, M. Biondi, O. Zilberberg, and R. Chitra, Quantum Transducer Using a Parametric Driven-Dissipative Phase Transition, *Phys. Rev. Lett.* **123**, 173601 (2019).
- [14] M. Foss-Feig, P. Niroula, J. T. Young, M. Hafezi, A. V. Gorshkov, R. M. Wilson, and M. F. Maghrebi, Emergent equilibrium in many-body optical bistability, *Phys. Rev. A* **95**, 043826 (2017).
- [15] A. Lucas, Ising formulations of many NP problems, *Front. Phys.* **2**, 5 (2014).
- [16] O. Kyriienko, H. Sigurdsson, and T. C. H. Liew, Probabilistic solving of NP-hard problems with bistable nonlinear optical networks, *Phys. Rev. B* **99**, 195301 (2019).
- [17] F. Barahona, On the computational complexity of Ising spin glass models, *J. Phys. A* **15**, 3241 (1982).
- [18] H. Risken, C. Savage, F. Haake, and D. F. Walls, Quantum tunneling in dispersive optical bistability, *Phys. Rev. A* **35**, 1729 (1987).
- [19] K. Vogel and H. Risken, Quasiprobability distributions in dispersive optical bistability, *Phys. Rev. A* **39**, 4675 (1989).
- [20] K. Vogel and H. Risken, Dispersive optical bistability for large photon numbers and low cavity damping, *Phys. Rev. A* **42**, 627 (1990).
- [21] C. K. Andersen, A. Kamal, N. A. Masluk, I. M. Pop, A. Blais, and M. H. Devoret, Quantum Versus Classical Switching Dynamics of Driven Dissipative Kerr Resonators, *Phys. Rev. Appl.* **13**, 044017 (2020).
- [22] H. Kramers, Brownian motion in a field of force and the diffusion model of chemical reactions, *Physica* **7**, 284 (1940).
- [23] Thermodynamics of radiation, *Modern Thermodynamics* (Wiley, New York, 2014), Chap. 11, pp. 287–303.
- [24] K. Sekimoto, Langevin equation and thermodynamics, *Prog. Theor. Phys.* **130**, 17 (1998).
- [25] C. Jarzynski, Equalities and inequalities: Irreversibility and the second law of thermodynamics at the nanoscale, *Annu. Rev. Condens. Matter Phys.* **2**, 329 (2011).
- [26] U. Seifert, Stochastic thermodynamics, fluctuation theorems and molecular machines, *Rep. Prog. Phys.* **75**, 126001 (2012).
- [27] S. Ciliberto, Experiments in Stochastic Thermodynamics: Short History and Perspectives, *Phys. Rev. X* **7**, 021051 (2017).
- [28] H. J. Carmichael, Breakdown of Photon Blockade: A Dissipative Quantum Phase Transition in Zero Dimensions, *Phys. Rev. X* **5**, 031028 (2015).
- [29] F. Minganti, A. Biella, N. Bartolo, and C. Ciuti, Spectral theory of Liouvillians for dissipative phase transitions, *Phys. Rev. A* **98**, 042118 (2018).
- [30] D. O. Krimer and M. Pletyukhov, Few-Mode Geometric Description of a Driven-Dissipative Phase Transition in an Open Quantum System, *Phys. Rev. Lett.* **123**, 110604 (2019).
- [31] X. H. H. Zhang and H. U. Baranger, Driven-dissipative phase transition in a Kerr oscillator: From semiclassical  $\mathcal{PT}$  symmetry to quantum fluctuations, *Phys. Rev. A* **103**, 033711 (2021).
- [32] A. Delteil, T. Fink, A. Schade, S. Höfling, C. Schneider, and A. Imamoglu, Towards polariton blockade of confined exciton-polaritons, *Nat. Mater.* **18**, 219 (2019).

- [33] G. Muñoz-Matutano, A. Wood, M. Johnsson, X. Vidal, B. Q. Baragiola, A. Reinhard, A. Lemaître, J. Bloch, A. Amo, G. Nogues *et al.*, Emergence of quantum correlations from interacting fibre-cavity polaritons, *Nat. Mater.* **18**, 213 (2019).
- [34] H. Abbaspour, S. Trebaol, F. Morier-Genoud, M. T. Portella-Oberli, and B. Deveaud, Stochastic Resonance in Collective Exciton-Polariton Excitations inside a GaAs Microcavity, *Phys. Rev. Lett.* **113**, 057401 (2014).
- [35] K. J. H. Peters, Z. Geng, K. Malmir, J. M. Smith, and S. R. K. Rodriguez, Extremely Broadband Stochastic Resonance of Light and Enhanced Energy Harvesting Enabled by Memory Effects in the Nonlinear Response, *Phys. Rev. Lett.* **126**, 213901 (2021).
- [36] A. A. P. Trichet, J. Foster, N. E. Omori, D. James, P. R. Dolan, G. M. Hughes, C. Vallance, and J. M. Smith, Open-access optical microcavities for lab-on-a-chip refractive index sensing, *Lab Chip* **14**, 4244 (2014).
- [37] C. Vallance, A. A. P. Trichet, D. James, P. R. Dolan, and J. M. Smith, Open-access microcavities for chemical sensing, *Nanotechnology* **27**, 274003 (2016).
- [38] M. H. Bitarafan and R. G. DeCorby, On-chip high-finesse Fabry-Pérot microcavities for optical sensing and quantum information, *Sensors* **17**, 1748 (2017).
- [39] S. R. K. Rodriguez, Enhancing the Speed and Sensitivity of a Nonlinear Optical Sensor with Noise, *Phys. Rev. Appl.* **13**, 024032 (2020).
- [40] K. J. H. Peters and S. R. K. Rodriguez, Exceptional Precision of a Nonlinear Optical Sensor at a Square-Root Singularity, *Phys. Rev. Lett.* **129**, 013901 (2022).
- [41] A. A. P. Trichet, P. R. Dolan, D. James, G. M. Hughes, C. Vallance, and J. M. Smith, Nanoparticle trapping and characterization using open microcavities, *Nano Lett.* **16**, 6172 (2016).
- [42] L. Fan, J. Wang, L. T. Varghese, H. Shen, B. Niu, Y. Xuan, A. M. Weiner, and M. Qi, An all-silicon passive optical diode, *Science* **335**, 447 (2012).
- [43] Y. Shi, Z. Yu, and S. Fan, Limitations of nonlinear optical isolators due to dynamic reciprocity, *Nat. Photonics* **9**, 388 (2015).
- [44] D. L. Sounas, J. Soric, and A. Alù, Broadband passive isolators based on coupled nonlinear resonances, *Nat. Electron.* **1**, 113 (2018).
- [45] S. R. K. Rodriguez, V. Goblot, N. C. Zambon, A. Amo, and J. Bloch, Nonreciprocity and zero reflection in nonlinear cavities with tailored loss, *Phys. Rev. A* **99**, 013851 (2019).
- [46] K. Y. Yang, J. Skarda, M. Cotrufo, A. Dutt, G. H. Ahn, M. Sawaby, D. Vercruysse, A. Arbabian, S. Fan, A. Alù *et al.*, Inverse-designed non-reciprocal pulse router for chip-based lidar, *Nat. Photonics* **14**, 369 (2020).
- [47] M. Cotrufo, S. A. Mann, H. Moussa, and A. Alù, Nonlinearity-induced nonreciprocity—Part I, *IEEE Trans. Microw. Theory Tech.* **69**, 3569 (2021).
- [48] X.-W. Xu, Y. Li, B. Li, H. Jing, and A.-X. Chen, Nonreciprocity via Nonlinearity and Synthetic Magnetism, *Phys. Rev. Appl.* **13**, 044070 (2020).
- [49] L. De Santis, C. Antón, B. Reznichenko, N. Somaschi, G. Coppola, J. Senellart, C. Gómez, A. Lemaître, I. Sagnes, A. G. White *et al.*, A solid-state single-photon filter, *Nat. Nanotechnol.* **12**, 663 (2017).
- [50] H. Snijders, J. A. Frey, J. Norman, V. P. Post, A. C. Gossard, J. E. Bowers, M. P. van Exter, W. Löffler, and D. Bouwmeester, Fiber-Coupled Cavity-QED Source of Identical Single Photons, *Phys. Rev. Appl.* **9**, 031002(R) (2018).
- [51] N. Tomm, A. Javadi, N. O. Antoniadis, D. Najer, M. C. Löbl, A. R. Korsch, R. Schott, S. R. Valentin, A. D. Wieck, A. Ludwig *et al.*, A bright and fast source of coherent single photons, *Nat. Nanotechnol.* **16**, 399 (2021).
- [52] P. D. Drummond and D. F. Walls, Quantum theory of optical bistability. I. Nonlinear polarisability model, *J. Phys. A* **13**, 725 (1980).
- [53] D. S. Lemons and A. Gythiel, Paul Langevin’s 1908 paper “On the theory of Brownian motion” [“sur la théorie du mouvement brownien,” *C. R. Acad. Sci. (paris)* 146, 530–533 (1908)], *Am. J. Phys.* **65**, 1079 (1997).
- [54] D. T. Gillespie, The mathematics of Brownian motion and Johnson noise, *Am. J. Phys.* **64**, 225 (1996).
- [55] A. C. Barato, E. Roldán, I. A. Martínez, and S. Pigolotti, Arcsine Laws in Stochastic Thermodynamics, *Phys. Rev. Lett.* **121**, 090601 (2018).
- [56] V. Ramesh, K. Peters, and S. Rodriguez, Arcsine laws of light, *arXiv:2208.07432*.
- [57] Z. Geng, K. J. H. Peters, A. A. P. Trichet, K. Malmir, R. Kolkowski, J. M. Smith, and S. R. K. Rodriguez, Universal Scaling in the Dynamic Hysteresis, and Non-Markovian Dynamics, of a Tunable Optical Cavity, *Phys. Rev. Lett.* **124**, 153603 (2020).
- [58] B. Garbin, A. Giraldo, K. J. H. Peters, N. G. R. Broderick, A. Spakman, F. Raineri, A. Levenson, S. R. K. Rodriguez, B. Krauskopf, and A. M. Yacomotti, Spontaneous Symmetry Breaking in a Coherently Driven Nanophotonic Bose-Hubbard Dimer, *Phys. Rev. Lett.* **128**, 053901 (2022).
- [59] S. Kiesewetter, R. Polkinghorne, B. Opanchuk, and P. D. Drummond, XSPDE: Extensible software for stochastic equations, *SoftwareX* **5**, 12 (2016).
- [60] E. Estrecho, T. Gao, N. Bobrovska, D. Comber-Todd, M. D. Fraser, M. Steger, K. West, L. N. Pfeiffer, J. Levinsen, M. M. Parish, T. C. H. Liew, M. Matuszewski, D. W. Snoke, A. G. Truscott, and E. A. Ostrovskaya, Direct measurement of polariton-polariton interaction strength in the Thomas-Fermi regime of exciton-polariton condensation, *Phys. Rev. B* **100**, 035306 (2019).
- [61] A. I. Lvovsky and M. G. Raymer, Continuous-variable optical quantum-state tomography, *Rev. Mod. Phys.* **81**, 299 (2009).
- [62] F. Arecchi, S. Boccaletti, and P. Ramazza, Pattern formation and competition in nonlinear optics, *Phys. Rep.* **318**, 1 (1999).
- [63] N. Moiseyev, *Non-Hermitian Quantum Mechanics* (Cambridge University Press, Cambridge, U.K., 2011).
- [64] W. D. Heiss, The physics of exceptional points, *J. Phys. A* **45**, 444016 (2012).
- [65] S. R.-K. Rodriguez, Classical and quantum distinctions between weak and strong coupling, *Eur. J. Phys.* **37**, 025802 (2016).
- [66] M.-A. Miri and A. Alù, Exceptional points in optics and photonics, *Science* **363**, eaar7709 (2019).
- [67] M. Soriente, T. L. Heugel, K. Omiya, R. Chitra, and O. Zilberberg, Distinctive class of dissipation-induced phase transitions and their universal characteristics, *Phys. Rev. Res.* **3**, 023100 (2021).

- [68] V. Y. Chernyak, M. Chertkov, and C. Jarzynski, Path-integral analysis of fluctuation theorems for general Langevin processes, *J. Stat. Mech. Theory Exp.* (2006) P08001.
- [69] R. Pan, T. M. Hoang, Z. Fei, T. Qiu, J. Ahn, T. Li, and H. T. Quan, Quantifying the validity and breakdown of the overdamped approximation in stochastic thermodynamics: Theory and experiment, *Phys. Rev. E* **98**, 052105 (2018).
- [70] K. P. Kalinin and N. G. Berloff, Polaritonic network as a paradigm for dynamics of coupled oscillators, *Phys. Rev. B* **100**, 245306 (2019).
- [71] D. Hunger, T. Steinmetz, Y. Colombe, C. Deutsch, T. W. Hänsch, and J. Reichel, A fiber Fabry-Pérot cavity with high finesse, *New J. Phys.* **12**, 065038 (2010).
- [72] A. A. P. Trichet, P. R. Dolan, D. M. Coles, G. M. Hughes, and J. M. Smith, Topographic control of open-access microcavities at the nanometer scale, *Opt. Express* **23**, 17205 (2015).
- [73] D. Bajoni, E. Peter, P. Senellart, J. L. Smirr, I. Sagnes, A. Lemaître, and J. Bloch, Polariton parametric luminescence in a single micropillar, *Appl. Phys. Lett.* **90**, 051107 (2007).
- [74] O. El Daïf, A. Baas, T. Guillet, J.-P. Brantut, R. I. Kaitouni, J. L. Staehli, F. Morier-Genoud, and B. Deveaud, Polariton quantum boxes in semiconductor microcavities, *Appl. Phys. Lett.* **88**, 061105 (2006).
- [75] I. Carusotto and C. Ciuti, Quantum fluids of light, *Rev. Mod. Phys.* **85**, 299 (2013).
- [76] E. Togan, H.-T. Lim, S. Faelt, W. Wegscheider, and A. Imamoglu, Enhanced Interactions between Dipolar Polaritons, *Phys. Rev. Lett.* **121**, 227402 (2018).
- [77] A. V. Zasedatelev, A. V. Baranikov, D. Sannikov, D. Urbonas, F. Scafirimuto, V. Y. Shishkov, E. S. Andrianov, Y. E. Lozovik, U. Scherf, T. Stöferle *et al.*, Single-photon nonlinearity at room temperature, *Nature (London)* **597**, 493 (2021).